metals

MDPI

Article

The Microstructure and Mechanical Property of 2024Al/W Materials with High W Content Fabricated by Lower-Temperature Sintering

Cunhui Jiang, Xiaoxuan Pang * and Liang Cheng *

Materials Research Institute, China Academy of Engineering Physics, Mianyang 621907, China; jch7528@163.com
* Correspondence: pxx3751@163.com (X.P.); mcchengliang@126.com (L.C.);
Tel.: +86-166-5960-9933 (X.P.); +86-166-5960-7726 (L.C.)

Abstract

Al-W composites are lightweight, high-strength, structural–functional integrated materials with tailorable density and excellent X/γ-ray shielding performance, making them promising candidates for nuclear and aerospace applications. In this study, high-W-content 2024Al-W composites were successfully fabricated via spark plasma sintering (SPS) at a relatively low temperature of 440–500 °C. With increasing sintering temperature, the relative density of the composites increased from 99.6% to 99.9%. A ternary intermetallic compound, $Al_{18}Mg_3W_2$, was first detected at the Al/W interface at 460 °C. At 480 °C, submicrometre $Al_{18}Mg_3W_2$ phases formed and cooperated with nanoscale Al_2Cu precipitates, effectively enhancing interfacial bonding and optimizing mechanical properties—yielding an ultimate tensile strength of 266.9 MPa and an elongation of 6.2%. Among the strengthening mechanisms, coefficient of thermal expansion (CTE) mismatch strengthening contributed the most (~19.2 MPa), followed by load transfer (~4.27 MPa) and Orowan strengthening (~1.17 MPa). These findings provide valuable insights into the low-temperature preparation of high-W-content Al-W structural–functional materials via SPS.

Keywords: aluminum tungsten composite material; preparation process; research progress; mechanical property

check for updates

Academic Editor: Massimo Pellizzari

Received: 13 September 2025
Revised: 14 October 2025
Accepted: 16 October 2025
Published: 24 October 2025

Citation: Jiang, C.; Pang, X.; Cheng, L. The Microstructure and Mechanical Property of 2024Al/W Materials with High W Content Fabricated by Lower-Temperature Sintering. *Metals* **2025**, *15*, 1176. https://doi.org/10.3390/met15111176

Copyright: © 2025 by the authors. Licensee MDPI, Basel, Switzerland. This article is an open access article distributed under the terms and conditions of the Creative Commons Attribution (CC BY) license (https://creativecommons.org/licenses/by/4.0/).

1. Introduction

Aluminum matrix composites (Al-MMCs) demonstrate immense promise in nuclear radiation shielding structures and aerospace lightweight load-bearing components, leveraging their low density and microstructural designability [1]. Among these, tungsten particle-reinforced Al-MMCs are ideal for balancing structural strength and radiation protection, combining tungsten's high density (19.3 g/cm^3), excellent radiation shielding properties [2,3], and the plastic deformation capability of the aluminum matrix. As an important tungsten-based alloy, Al-W alloy effectively combines the advantages of both tungsten and aluminum [4].

Aluminum- tungsten alloys are predominantly utilized in applications including golf club heads, medical equipment components, automotive engine pistons, wheel hubs, and various other components; they are also anticipated to be employed in armour materials and aerospace engines, among others. The 2024 aluminum alloy primarily consists of aluminum, copper, magnesium, iron, silicon, and manganese. It exhibits high strength, good plastic toughness, excellent fatigue resistance, corrosion resistance, and outstanding hot and cold-machining properties [5–9].

However, 2024Al/W composites prepared via conventional processes (e.g., casting, hot extrusion) face two key bottlenecks: first, the extremely low solid solubility of tungsten in aluminum tends to induce the formation of brittle intermetallic compounds (e.g., $Al_{12}W$, Al_5W, Al_4W) at elevated temperatures; second, the agglomeration of tungsten particles (especially micrometre- scale ones) in conventional processes easily causes stress concentration, leading to a significant reduction in composite ductility. Currently, common preparation methods for Al-W composites include hot press sintering, extrusion moulding, discharge plasma sintering, high- current pulsed electron beam, sputtering deposition, accumulative roll bonding, friction stir processing, etc. [10–16]. Among these, SPS shows significant technological advantages such as rapid heating rates, uniform thermal processes, short sintering durations, low required sintering temperatures, and high production efficiency. Meanwhile, this technique not only ensures homogeneous microstructures of products and preserves inherent properties of raw materials but also facilitates the fabrication of high-density materials and complex-shaped workpieces [17].

To meet the unresolved challenges in Al-W composite development and advance beyond the current state of the art (Table 1), this study delivers three quantifiable leaps that close critical gaps in the literature:

Table 1. Properties of Al- W composites prepared by various processes.

Process	Composition	Tensile Strength	Elongation	Vickers Hardness	Reference
Extrusion	Al-0.71 wt.% W	478 MPa	15.4%	/	[11]
Hot-pressing sintering	Al-3vol.%W	200 MPa	7.3%	/	[10]
Spark plasma sintering	Al-50 wt.%W- 1 wt.%B	240.2 MPa	13%	/	[18]
Accumulative roll bonding	Al-4.2 vol.%W	160 MPa	/	59.98 HV	[14]
Friction stir processing	Al-3.6 vol.%W	210 MPa	/	65 HV	[4]

Performance leap: For the first time, 2024Al-40 wt % W achieved > 99.9% relative density at $\leq$480 °C without additives; the resulting 266.9 MPa UTS and 6.2% elongation surpass hot-pressed [10] and SPS [18] values while retaining practical ductility, ending the strength–ductility–W-content trade-off.

Process leap: By exploiting 2024Al intrinsic age-hardening and optimized SPS parameters (100 °C min^{-1}, 10 min dwell), we suppress brittle $Al_{12}W/Al_5W$ formation and W coarsening; a hierarchical reinforcement (micro-W, sub-μm $Al_{18}Mg_3W_2$ and nano Al_2Cu) is obtained in high-W Al-MMCs for the first time.

Interface leap: In situ nucleation of ternary $Al_{18}Mg_3W_2$ at the Al/W interface ($\geq$460 °C) is detected for the first time in an Al-W system; together with nano Al_2Cu, it relieves thermal-mismatch stress and strengthens interfacial bonding—an effect rarely reported since previous studies [11,14] focused on dispersion rather than interface engineering.

These advances provide a scalable, energy-efficient route to high-W Al-MMCs that integrate structural load-bearing with radiation-shielding functionality, pushing Al-W composites beyond the current ceiling (Table 1) for nuclear and aerospace applications.

2. Materials and Methods

Commercial 2024 aluminum powder (Hunan Aoke New Materials Technology Co., Ltd., Changsha, China) with a particle size of 510 μm and a purity $\geq$ 99.8% was used as the matrix. Its nominal composition (wt %) is Al 91.592.5, Cu 4.04.5, Mg 1.41.6, Mn 0.50.7, and $\leq$0.15 impurities. Spherical tungsten powder (D50 = 10.1 μm, purity $\geq$ 99.95%, Hebei Hongju Metal Materials Co., Ltd., Cangzhou, China) served as the reinforcement. The two powders were weighed to give a 6:4 2024Al:W mass ratio and blended by planetary ball

milling (QM-3SP4, Nanjing Nanda Instrument Factory, Nanjing, China). Five grams of the mixed powder and 50 g of agate balls (5 and 10 mm in diameter, 1:1 by mass, ball-to-powder mass ratio 10:1) were loaded into a 100 mL agate jar inside a glove box, which was then evacuated and back-filled with 99.999% pure Ar to prevent oxidation. Milling was performed at 200 rpm (revolution) and 400 rpm (rotation) for 6 h; preliminary trials confirmed that this protocol yields homogeneous mixing without noticeable powder fracture.

The composite powder was immediately consolidated by SPS using a graphite die (Ø 12.2 mm, purity 99.9%). A uniaxial pressure of 30 MPa was applied under flowing Ar. The pulse pattern was 12 ms on/2 ms off, one pulse per cycle, with no dwell between pulses. Samples were heated at 100 °C min^{-1} to 440, 460, 480 or 500 °C and held for 600 s, producing cylindrical discs 12.2 mm in diameter and ~5 mm thick (mass ≈ 2.45 g).

After sintering, the discs were ground sequentially with SiC paper (400–2000 grit) and polished to a mirror finish with 1 μm diamond paste. Microstructural observation and fracture analysis were conducted in back-scattered electron (BSE) mode using a JEOL JSM-7200F SEM (JEOL Ltd., Tokyo, Japan)operated at 5 kV. Elemental distributions were mapped with an Oxford X-Max energy-dispersive spectrometer (EDS) at 5 kV, 140 keV acquisition window; area scans lasted 120 s, point spectra 30 s, and line scans were acquired every 0.1 μm with 5 s per point. Energy calibration employed a Co standard; attention was focused on Al/W interfacial chemistry, the composition of the $Al_{18}Mg_3W_2$ phase and associated concentration gradients.

Phase identification was performed on a Rigaku SmartLab SE X-ray diffractometer (Cu Kα, λ = 0.154 nm, 2θ = 10–90°, step 0.02°). Tensile properties were measured at 2 mm min^{-1} with an Instron 8862 universal tester. Dog-bone specimens had a 10 × 3.5 × 2 mm^3 gauge section, 2 mm fillet radius and 28 mm total length; three samples per condition were tested and averaged. Thermal behaviour was examined in a Netzsch STA 449 F5 DSC(Netzsch-Gerätebau GmbH, Selb, Germany) under 50 mL min^{-1} Ar (251,000 °C, 10 K min^{-1}). Ten milligram samples of as-milled powder and 480 °C sintered material were placed in Al_2O_3 crucibles and baseline-corrected to identify Al melting endotherms and interfacial reaction exotherms. Bulk density was obtained by the Archimedes method using an electronic balance. Foils ~50 μm thick were prepared by mechanical grinding and examined in an FEI Talos F200X field-emission (Thermo Fisher Scientific, Waltham, MA, USA) TEM to reveal nanometre-scale interfacial structures.

In this study, the key processing parameters for preparing 2024Al/W composites via SPS were determined based on preliminary screening. The sintering pressure was fixed at 30 MPa, as lower pressures yielded insufficient densification, while higher pressures improved density by <0.2% and risked die wear and stress cracking of the sample. The dwell time was set at 600 s; shorter times led to inadequate particle diffusion and low density, whereas longer times promoted excessive agglomeration of the $Al_{18}Mg_3W_2$ ternary phase and degraded mechanical properties. Consequently, the formal experiments employed "30 MPa + 600 s" as the baseline, with only the sintering temperature being varied (440 °C, 460 °C, 480 °C, 500 °C) to isolate its influence on microstructural evolution and mechanical performance.

3. Results and Discussion

3.1. Densification Behaviour as a Function of Sintering Temperature

Sintering temperature, holding time, and pressure synergistically affect densification [19–24]. In this study, with holding time (600 s) and pressure (30 MPa) fixed, we focused on the effect of sintering temperature on the density of 2024Al/W composites (Table 2). Table 2 presents density data of 2024Al/W composites sintered at different temperatures under constant holding time and pressure. The results show that measured density

increased progressively with sintering temperature, approaching the theoretical density (4.2140 g/cm^3) from 4.1986 g/cm^3 at 440 °C to 4.2128 g/cm^3 at 500 °C. Correspondingly, relative density rose continuously, reaching 99.6% at 440 °C, 99.7% at 460 °C, and 99.9% at 480 °C and 500 °C.

Table 2. Density of 2024Al/W composites prepared at different temperatures.

Temperature/°C	Measured Density/g·cm^{-3}	Theoretical Density/g·cm^{-3}	Relative Density/%
440	4.1986	4.2140	99.6
460	4.2031	4.2140	99.7
480	4.2114	4.2140	99.9
500	4.2128	4.2140	99.9

At 440 °C, the relative density of 99.6% indicates pronounced densification driven by interparticle diffusion and pore shrinkage during initial sintering. At 460 °C, the slight increase to 99.7% demonstrates that higher temperatures enhance atomic activity, accelerating pore filling. Notably, relative densities of 99.9% were achieved at 480 °C and 500 °C, approaching theoretical density. This indicates that elevated temperatures provide sufficient kinetic energy for atomic diffusion, promoting complete pore filling in the material. These findings confirm that increasing sintering temperature enhances atomic diffusion kinetics, effectively reducing internal porosity and improving densification.

3.2. Phase Evolution and Microstructural Development

3.2.1. Phase Composition Analysis

Figure 1 presents the X-ray diffraction (XRD) patterns of 2024Al/W composites sintered at various temperatures. When the sintering temperature reached 460 °C, characteristic reflections of the ternary $Al_{18}Mg_3W_2$ phase (cubic, space group Fd-3m) emerged for the first time; no signals attributable to this phase were detected in the sample processed at 440 °C. In contrast, distinct peaks of the Al_2Cu binary phase (tetragonal, space group I4/mcm) were present in all patterns recorded between 440 and 500 °C, confirming that Al_2Cu remains a thermodynamically stable secondary phase throughout this temperature window. With increasing temperature, the intensities of the Al and W reflections decreased to different extents, reflecting changes in phase content and improved crystal perfection resulting from enhanced atomic diffusion.

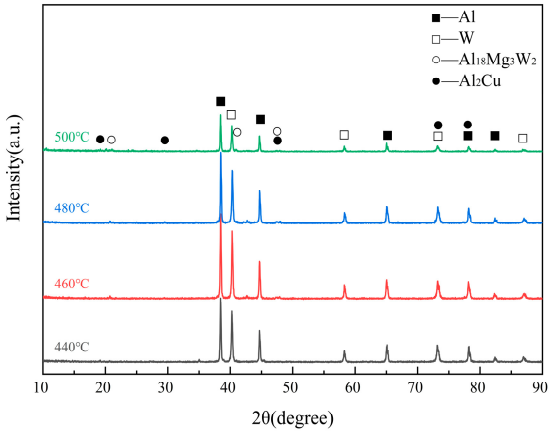


Figure 1. X-ray diffraction (XRD) characterization results of 2024 Al/W composites sintered at different temperatures.

3.2.2. Microstructural Characteristics

Figure 2 shows backscattered electron (BSE) SEM micrographs and EDS maps acquired from the interface region of the 2024Al/W composite. In Figure 2a the Al matrix appears dark, whereas W particles appear bright; the two phases are in intimate contact, and no pores or microcracks are observed. A continuous grey reaction layer ~4 μm thick is visible along the Al/W boundary. EDS mapping (Figure 2b–d) reveals limited mutual interdiffusion of Al and W, a pronounced Mg enrichment at the interface, and a heterogeneous Cu distribution (present both at the interface and within the matrix). Point analysis (Figure 2g) indicates that the grey layer contains Al, Mg, W, Cu and a small O signal. Taken together with the XRD results (Figure 1), which show $Al_{18}Mg_3W_2$ and Al_2Cu reflections, the grey layer is inferred to consist mainly of these two intermetallic phases, with the oxygen signal probably arising from trace Al_2O_3.

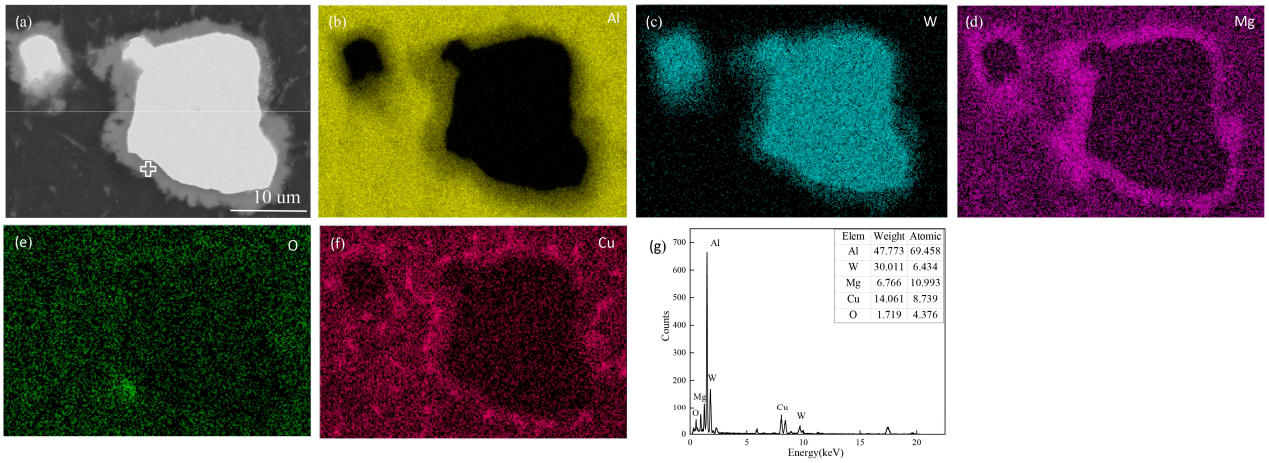


Figure 2. Backscattered electron (BSE) image and energy-dispersive X-ray spectroscopy (EDS) maps of the 2024Al/W composite interface: (**a**) BSE micrograph; (**b**–**f**) elemental distribution maps for Al, W, Mg, O and Cu, respectively; (**g**) EDS point analysis spectrum acquired from the reaction layer. The cross symbol in (**a**) represents the specific location of EDS point analysis in (**g**).

Figure 3 presents backscattered SEM images of 2024Al/W composites at different reaction temperatures. Low-magnification SEM images (Figure 3a,c,e,g) show uniform distribution and excellent dispersion of W phase particles in the Al matrix. High-magnification SEM images (Figure 3b,d,f,h) reveal significant variations in W phase particle sizes and boundary characteristics with temperature. At 440 °C, W phase particles are larger with well-defined, clear boundaries (Figure 3b). At other temperatures, particle size decreases and boundaries become irregular and indistinct (Figure 3h), indicating that elevated temperatures promote phase transformation.

EDS line scan profiling was employed to quantify the thickness of the interfacial reaction products. Figure 4a reveals that a sub micrometre layer formed at 480 °C, exhibiting an average thickness of 1.004 μm and a local maximum of 2.017 μm. After sintering at 500 °C, the reaction layer became lamellar and significantly thicker, with an average value of 3.701 μm and local peaks up to 4.761 μm.

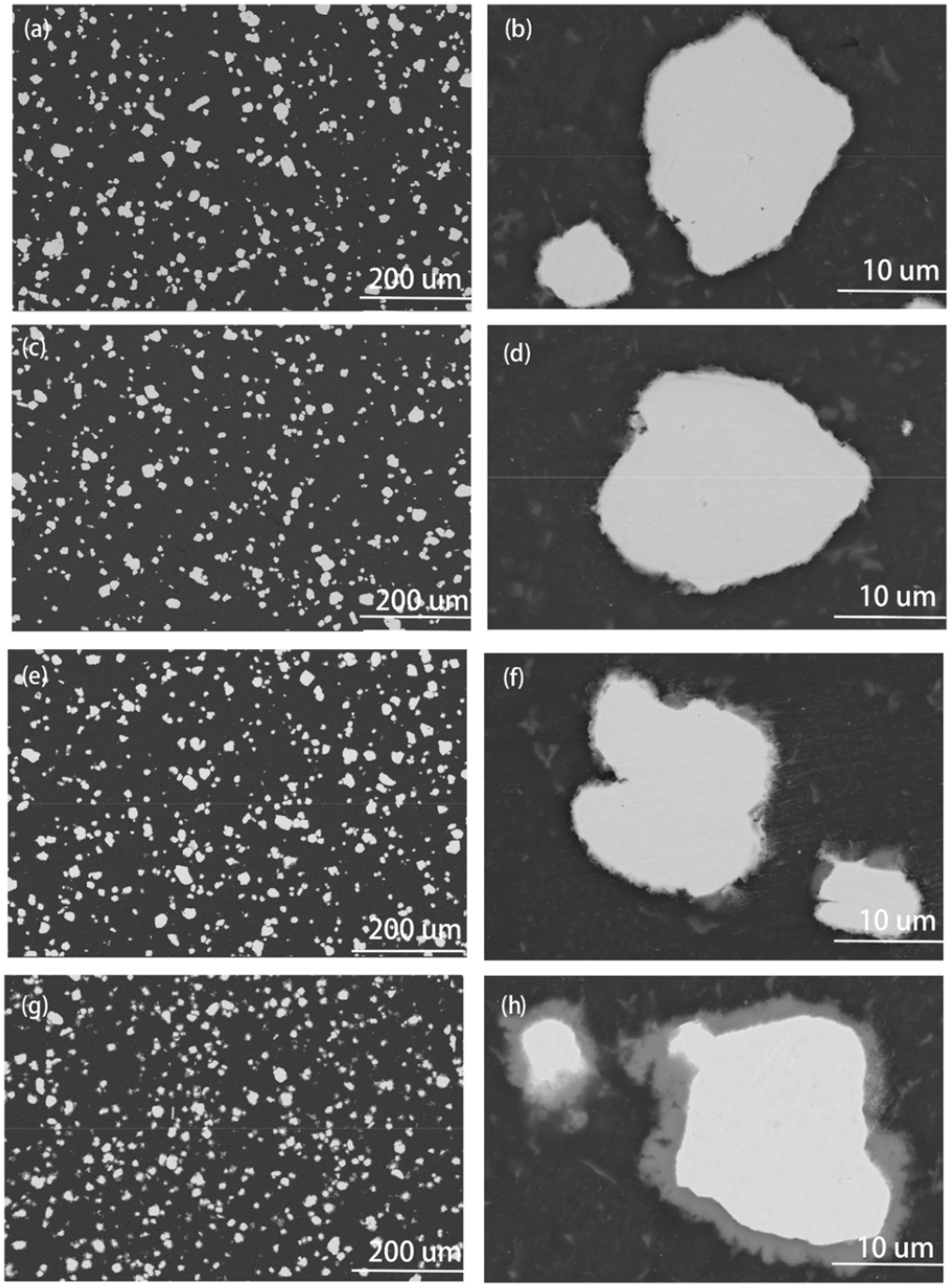


Figure 3. Backscattered SEM images of 2024 Al/W composites at different processing temperatures. (**a**,**c**,**e**,**g**) are low-magnification SEM images at 440 °C, 460 °C, 480 °C, and 500 °C; (**b**,**d**,**f**,**h**) are corresponding high-magnification SEM images.

To corroborate the crystal structure of the interfacial phases, a TEM foil prepared from the 480 °C sintered specimen was examined by high-resolution transmission electron microscopy (HRTEM) and selected-area electron diffraction (SAED); the results are summarized in Figure 5. Figure 5a–d present HRTEM images acquired at increasing magnification from the reaction zone, while Figure 5e–h display the SAED patterns recorded from the circled regions d–g in Figure 5b–d. Indexing of the patterns reveals that the layer adjacent to the W particle is face-centred-cubic (fcc) $Al_{18}Mg_3W_2$ (Figure 5b,e), whereas the band on the Al side is body-centred-tetragonal (bct) Al_2Cu (Figure 5b,f). The pattern in Figure 5c corresponds to rhombohedral Al_2O_3, confirming that fragments of the native alumina film

remain at the Al/W boundary (Figure 5g). The diffuse rings in Figure 5d are again indexed as bct Al_2Cu, evidencing nanometre-scale Al_2Cu precipitates dispersed throughout the matrix. The residual Al_2O_3 film acts as a kinetic barrier to direct Al-W reaction; wherever this film is locally disrupted, rapid Mg diffusion permits the formation of fcc $Al_{18}Mg_3W_2$, which nucleates preferentially on the W surface (Figure 5b,e). Subsequently, Al and Cu atoms segregate at the $Al_{18}Mg_3W_2$ periphery and within the supersaturated matrix, giving rise to tetragonal Al2Cu precipitates (Figure 5b,h) that further strengthen the composite via Orowan and precipitation mechanisms.

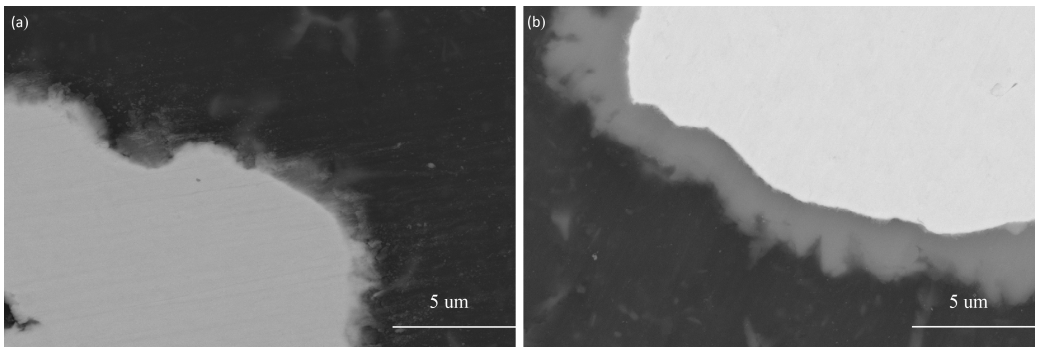


Figure 4. High-magnification backscattered electron scanning electron microscope (SEM) images of 2024Al/W composites subjected to different reaction temperatures: (**a**) 480 °C; (**b**) 500 °C.

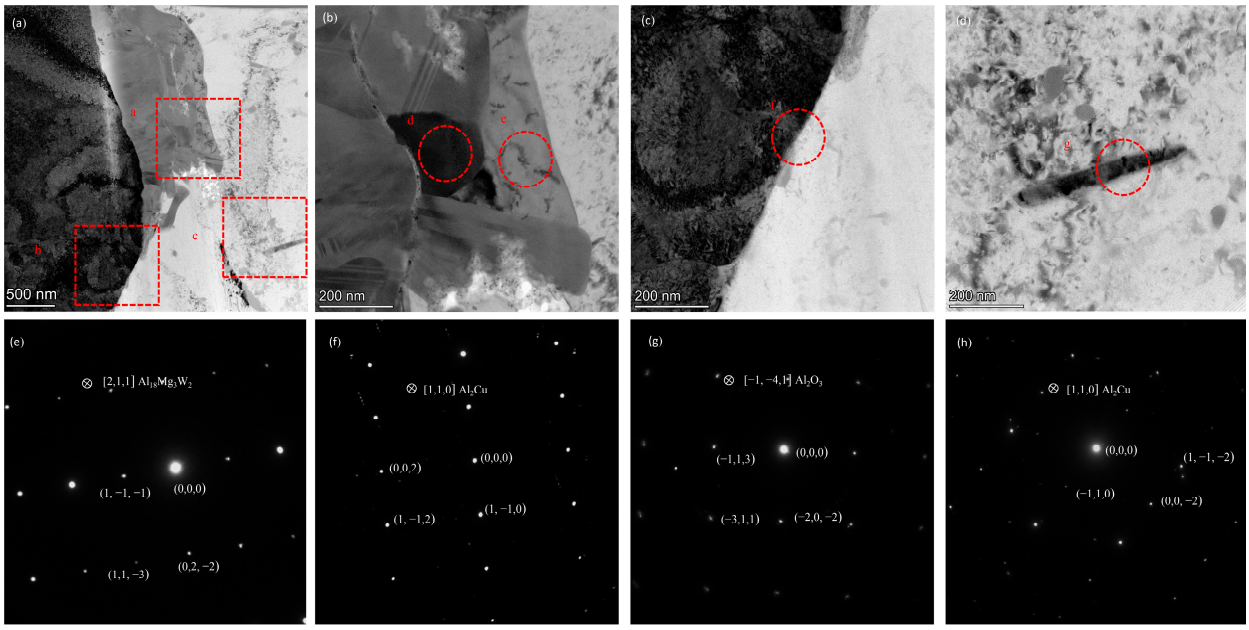


Figure 5. (**a**) HAADF-STEM overview of the 2024Al/W interface, with red rectangles a–c indicating the characterization regions; (**b**) HRTEM image corresponding to red rectangle a in (**a**), showing the high-resolution microstructure of the Al-W interface reaction zone; (**c**) HRTEM image corresponding to red rectangle b in (**a**), displaying the high-resolution microstructure at the Al-W grain boundary; (**d**) HRTEM image corresponding to red rectangle c in (**a**), illustrating the high-resolution microstructure of precipitated phases in the Al matrix; (**e**) SAED pattern acquired from red circle d in (**b**), corresponding to face-centered cubic (FCC) $Al_{18}Mg_3W_2$; (**f**) SAED pattern obtained from red circle e in (**b**), corresponding to tetragonal Al_2Cu; (**g**) SAED pattern collected from red circle f in (**c**), corresponding to Al_2O_3 at the Al-W grain boundary; (**h**) SAED pattern captured from red circle g in (**d**), corresponding to dispersed Al_2Cu phases in the Al matrix.

3.3. Interfacial Reaction Pathway and Phase Formation Mechanism

In the differential scanning calorimetry (DSC) tests, the enthalpy change was obtained by integrating the heat-flow curve over the characteristic temperature interval (from the onset to the endset of each peak), allowing a quantitative evaluation of the thermal effects associated with phase transformations and chemical reactions. Figure 6 compares the DSC traces of the powder (blue curve) and sintered bulk (red curve); the main thermal events are interpreted as follows. For the powder sample (blue), the pronounced endotherm at 644.3 °C ($\Delta H = 139.7$ J g^{-1}) corresponds to the melting of the aluminum matrix. The strong exotherm at 931.1 °C ($\Delta H = 899.9$ J g^{-1}) is ascribed to the formation of Al-W intermetallics when molten Al comes into intimate contact with W particles at high temperature; because the powder has not been sintered, the Al/W interface area is large and the reaction is vigorous. The decrease in atomic binding energy during compound formation releases a considerable amount of heat [25]. For the bulk specimen (red), the series of weak exotherms around 600 °C (peaks A, B, C) reflect solid-state reactions between Al, W and Mg that produce $Al_{18}Mg_3W_2$, $Al_{12}W$ and related phases. Peak C is smaller because partial $Al_{12}W$ was already formed during the preceding sintering step, leaving less reactant. Peak D, centred near 697 °C, is tentatively assigned to the melting of $Al_{12}W$ (m.p. ≈ 697 °C). The minor endotherm E at 910.3 °C ($\Delta H = 40.6$ J g^{-1}) originates from the melting of residual Al-based eutectic; its low enthalpy is consistent with the small volume fraction of this phase. Al_2O_3, whose melting point is ~2054 °C, is thermally stable and shows no peaks within the scanned temperature range, while the expected dissolution signal of Al_2Cu (300–500 °C) is not clearly resolved.

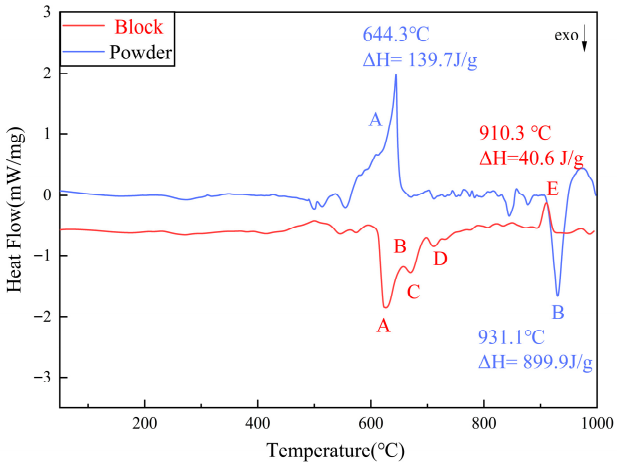


Figure 6. DSC curves of 2024Al/W composite and powder sintered at 480 °C.

Solid-state reaction between Al and W is hindered by a high energy barrier arising from their negligible mutual solubility and strong chemical affinity [26]; consequently, the formation of the ternary $Al_{18}Mg_3W_2$ phase at low temperatures is critically dependent on Mg addition. This facilitating effect can be rationalized from both thermodynamic and kinetic viewpoints: (1) Mg lowers the overall free energy of the system, rendering the ternary compound the most stable product; (2) Mg possesses a low melting point (~650 °C) and a high diffusion coefficient. At temperatures below the Al melting point, the solid-state interdiffusion coefficient between Al and refractory W (~3422 °C) is extremely small, so intermetallic formation is virtually impossible [27,28]. Mg acts as a highly mobile "transport medium" that enhances the overall atomic mobility, promotes mutual interaction between Al and W, and accelerates nucleation of $Al_{18}Mg_3W_2$. Additionally, the strong chemical affinity between Mg and Al favours the formation of Mg-rich intermetallics. Since the Al-Mg eutectic reaction already occurs at ~450 °C [29], minute amounts of Al-Mg liquid

or low-melting eutectic can form locally at the interface. This transient liquid provides a rapid diffusion path for W atoms [30], bypassing the high activation energy required for direct solid-state Al-W reaction and thereby enabling the synthesis of stable $Al_{18}Mg_3W_2$ at relatively low temperatures.

3.4. Mechanical Properties and Fracture Behaviour

Tensile tests were conducted to characterize the mechanical properties of 2024Al/W composites sintered at varying temperatures, with results presented in Figure 7. Correlation with densification data (Table 2) reveals that specimens sintered at 440 °C exhibit insufficient sintering driving force, leading to inadequate interparticle bonding and elevated residual porosity. These microstructural deficiencies result in lower tensile strength and elongation compared to composites processed at higher temperatures, as insufficient atomic diffusion at lower temperatures limits neck formation between particles and inhibits effective load transfer. Elevating the sintering temperature to 460 °C promotes densification, reduces porosity, and strengthens interfacial bonding—resulting in a significant simultaneous improvement in tensile strength and elongation compared to the 440 °C condition. This enhancement arises from increased atomic mobility at higher temperatures, facilitating more complete pore elimination and stronger metallurgical bonding at particle interfaces. Sintering at 480 °Cidentified as the optimal temperature—achieves near-theoretical density with tailored interfacial bonding, resulting in the maximum tensile strength and elongation values observed in this study. At this temperature, the balance between densification and grain growth is optimized, minimizing porosity while maintaining a fine-grained microstructure that contributes to both strength and ductility. At 500 °C, however, excessive sintering induces deleterious microstructural changes including grain coarsening, secondary pore formation, and interfacial degradation. These phenomena arise from accelerated grain boundary migration, localized element volatilization, and thermally activated recrystallization—collectively reducing tensile strength despite a marginal increase in elongation. The slight ductility improvement may stem from reduced stress concentration at fracture initiation sites due to coarser microstructure, though this effect is offset by compromised interfacial integrity.

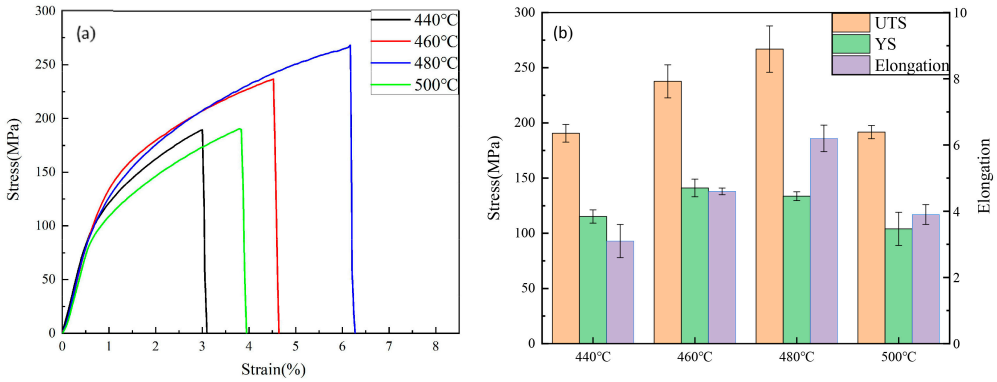


Figure 7. Tensile experimental results for 2024Al/W materials: (**a**) tensile stress–strain curve; (**b**) statistical results. UTS = ultimate tensile strength; YS = yield strength.

The Al-Mg-W ternary phase is believed to be a critical strengthening contributor: a moderate volume fraction of finely dispersed $Al_{18}Mg_3W_2$ particles enhances Al/W interfacial bonding and alleviates stress concentration, thereby simultaneously improving strength and ductility. When the ternary phase is allowed to overgrow or agglomerate at higher temperatures, it forms lamellar brittle zones that act as crack-initiation sites, causing a loss in strength. This trend is consistent with Figure 4a: at 480 °C only a faint interfacial reaction occurs, producing submicrometre reaction products that strengthen the

W/Al interface. In contrast, Figure 4b shows that at 500 °C an extensive interfacial reaction generates micrometre-scale, plate-like products that are detrimental to the overall strength.

Tensile fracture surfaces of 2024Al/W composites processed at different sintering temperatures were examined by scanning electron microscopy (SEM). All specimens exhibited dimpled rupture, but the population, size and depth of the dimples varied markedly with temperature. In the 440 °C sample (Figure 8a,b) only shallow dimples and scarce tear ridges were visible, together with microvoids and isolated W particles. This limited ductility is attributed to the low sintering temperature: the native Al_2O_3 film remained largely intact, $Al_{18}Mg_3W_2$ had not yet formed, and interfacial bonding between W and Al was weak, while incomplete powder consolidation left an only partially continuous matrix. Specimens sintered at 480 °C and 500 °C revealed pronounced ductile fracture. Extensive tear ridges and deep, uniformly distributed dimples covered the surface, giving a much rougher morphology. Many W particles were either fractured or pulled out, indicating efficient load transfer across a strongly bonded interface. The improved cohesion is ascribed to progressive rupture of the Al_2O_3 film and the synergistic action of $Al_{18}Mg_3W_2$ and Al_2Cu, which jointly strengthen the Al/W interface and enhance matrix continuity, thereby simultaneously increasing strength and ductility.

Collectively, the dominant strengthening and toughening mechanisms operating in 2024Al/W composites originate from two mutually reinforcing sources. First, the robust interfacial bonding between the reinforcing W particles and the Al matrix enables efficient load transfer from the comparatively soft matrix to the high-strength tungsten phase. During fracture, once the W ligaments are fully loaded and ultimately debond or break, the crack either propagates along the W/Al interface (interface debonding) or is deflected around the particles (crack deflection). Both processes lengthen the crack path and dissipate a considerable amount of fracture energy, markedly enhancing toughness and crack-growth resistance. Second, the intermetallic $Al_{18}Mg_3W_2$ formed in situ improves interfacial cohesion, while nanoscale Al_2Cu precipitates provide dispersion strengthening of the Al matrix; together these phases generate a synergistic reinforcement effect. Previous investigations have identified three micromechanical roles played by W particles within the Al matrix [31]: (1) The large thermal expansion mismatch between the Al matrix (23.86×10^{-6} K^{-1}) and W particles (4.5×10^{-6} K^{-1}) generates geometrically necessary dislocations and a residual stress field that strengthens the composite. (2) The intrinsically harder W particles impede plastic flow of the softer Al, elevating the overall dislocation density at the matrix–reinforcement interface. (3) During tensile loading the W ligaments act as rigid barriers that blunt and arrest propagating cracks. All three effectsthermal stress, increased dislocation density, and crack-blocking—scale with W content, leading simultaneously to higher strength and improved ductility in Al-W composites.

3.5. Synergistic Strengthening and Toughening Analysis

2024Al/W composites, as typical particle reinforced metal matrix composites (MMCs), achieve enhanced mechanical properties through the synergistic effects of multiple strengthening mechanisms induced by micron-sized tungsten (W) particles. The total strength increment can be predicted by summing contributions from individual mechanisms, as described below [32].

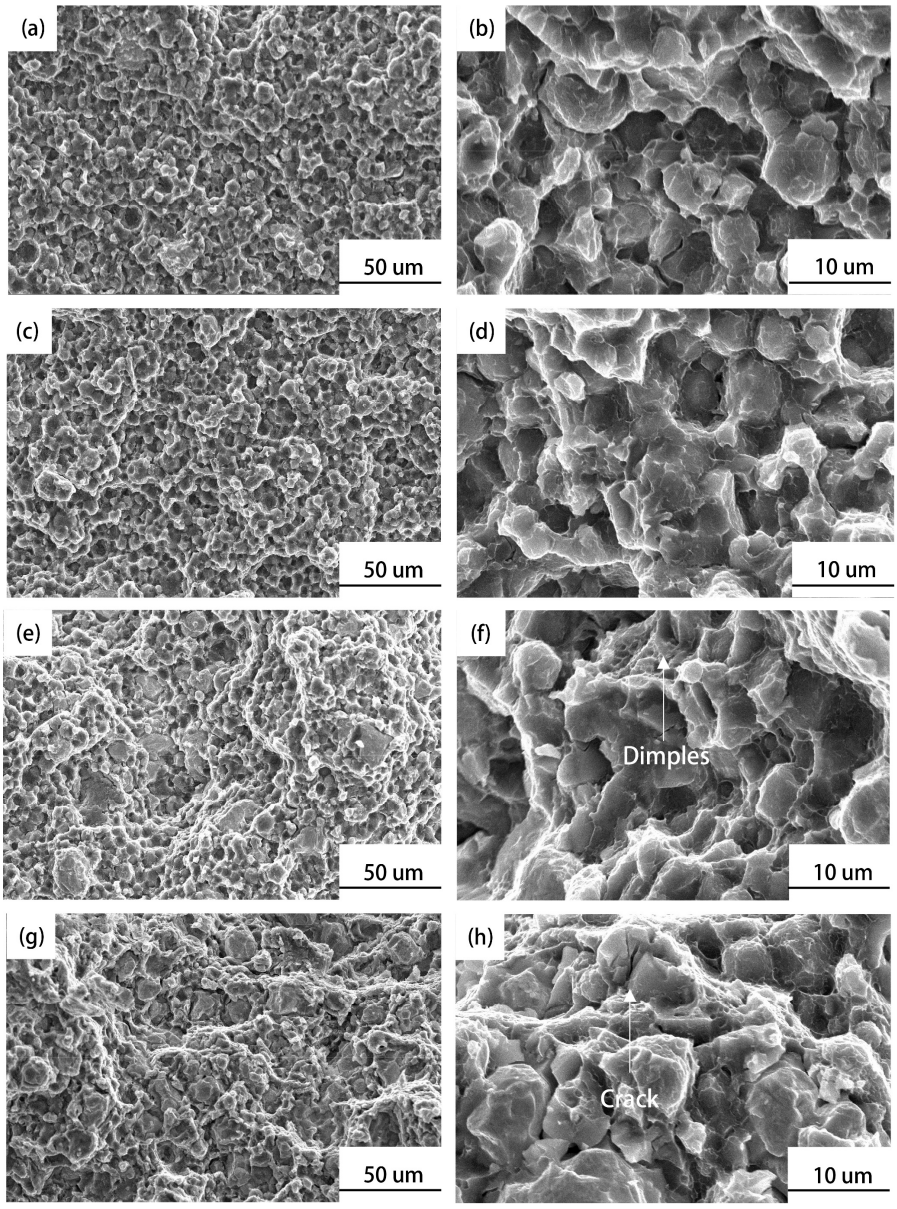


Figure 8. Fracture morphology of 2024 Al-40W composites subjected to tensile testing at different reaction temperatures: (**a**) 440 °C; (**c**) 460 °C; (**e**) 480 °C; (**g**) 500 °C; (**b**,**d**,**f**,**h**) are the corresponding high-magnification images.

3.5.1. Orowan Strengthening

The introduction of second phase particles is a key method to enhance material strength. In Al-W composites, aluminum powders or certain formed Al-W intermetallic compounds can act as the second phase. When these second phase particles reach the nanoscale, they effectively hinder dislocation motion and grain boundary migration. Owing to the high hardness and resistance to plastic deformation of the second phase, dislocation lines cannot cut through these particles but have to curve around them, forming dislocation loops [33]. This process, termed Orowan strengthening, contributes to the overall strengthening of the material. In the strengthening mechanism of metal matrix composites, the Orowan effect plays a critical role, especially when hard particles are closely

distributed and impede dislocation transmission. The strength increment caused by this mechanism can be described by the following equation:

$$\Delta\sigma_{\text{Orowan}} = \frac{0.13 G_m b}{\lambda} \ln \frac{d_p}{2b} \quad (1)$$

where $\Delta\sigma$ is the increment in yield strength due to the Orowan mechanism, G_m is the shear modulus of the matrix, d_p is the average particle size, b is the Burgers vector of the matrix, and λ is the average interparticle distance between the reinforcing particles [34]:

$$\lambda \approx d_p \left[\left(\frac{1}{2V_p} \right)^{\frac{1}{3}} - 1 \right] \quad (2)$$

The relevant parameters for 2024Al are as follows: shear modulus of 27.0 GPa [35], Burgers vector of 0.286 nm [35], and interparticle distance of approximately 7.98 μm. Based on these parameters, the Orowan strengthening contribution of W particles is estimated to be approximately 1.23 MPa. This value indicates that the Orowan strengthening mechanism is not the primary strengthening factor in the 2024Al-40wt.%W composite. Although the Orowan strengthening formula (OSF) can calculate the strengthening contribution of W particles to the 2024Al matrix, the deviation between the calculated results and actual measured values shows that this mechanism cannot fully predict the strengthening effect of W on the 2024Al matrix. This is mainly due to several limitations of the OSF: (1) it assumes either a single reinforcing particle phase or multiple particles with similar mechanical properties; (2) it does not consider the effects of particle size and distribution state. It should be noted that in metal matrix composites reinforced by micronsized particles, the Orowan strengthening effect is insignificant because of the coarser particle size and larger interparticle spacing.

To address the aforementioned limitation, we invoke the "discrete element method (DEM) particle distribution calibration model" advanced by Lupo et al. [36] and introduce a particle distribution uniformity correction factor, f, defined as the normalized deviation between the actual and an ideal uniform spatial distribution of precipitates. Consequently, the classical Orowan strengthening equation is modified as

$$\Delta\sigma_{\text{Orowan,corrected}} = \Delta\sigma_{\text{Orowan}} f \quad (3)$$

The factor f was quantified by statistically analyzing backscattered SEM micrographs: the distribution is most uniform after ageing at 480 °C (f = 0.95), whereas f = 0.72 at 440 °C and f = 0.81 at 500 °C. After correction, the Orowan increment at 480 °C becomes $1.23 \times 0.95 \approx 1.17$ MPa, markedly improving consistency with the contributions from other strengthening mechanisms. Lupo et al. demonstrated that the DEM framework accurately captures the statistical signature of particle distributions; incorporating the uniformity correction therefore remedies the conventional equations' inherent neglect of microscopic spatial heterogeneity. The present study validates the effectiveness of this refinement.

3.5.2. Thermal Mismatch Strengthening

The coefficient of thermal expansion (CTE) of tungsten is significantly lower than that of aluminum, with values of approximately 4.5×10^{-6} K^{-1} and 23.86×10^{-6} K^{-1}, respectively [37], representing an order-of-magnitude difference. During thermal cycles, this CTE mismatch induces internal stresses in the composite, a phenomenon termed thermal mismatch. Such thermal mismatch generates plastic residual strains, leading to

increased dislocation density and thus enhanced composite strength [38]. This relationship can generally be expressed as:

$$\Delta\sigma_{CTE} = k\, G_m b \sqrt{\rho} \quad (4)$$

where $\Delta\sigma_{CTE}$ represents the increase in strength attributable to thermal mismatch strengthening, k is a constant with a value of approximately 1.25, ρ is the dislocation density within the composite after the strengthening process, G_m is the shear modulus (MPa) of the metal matrix, and b is the Burgers vector of the matrix material. The dislocation density ρ within an isometric crystal can be calculated using the following equation:

$$\rho = \frac{12\, V_p \Delta\alpha \Delta T}{b\, d_p (1 - V_p)} \quad (5)$$

where V_p represents the particle volume fraction, $\Delta\alpha$ is the difference in the coefficient of thermal expansion between the aluminum matrix and the tungsten particles, and ΔT is the temperature difference from the processing temperature to room temperature. The thermal mismatch stress ($\Delta\sigma$CTE) between aluminium and tungsten was calculated to be about 17.89 MPa.

Conventional thermal mismatch strengthening models assume a uniform, agglomerate free dispersion of particles; however, W particles inevitably undergo various degrees of clustering during sintering, producing an inhomogeneous local stress field. To quantify the clustering effect, we adopt the "DEM particle agglomeration simulation" proposed by Lupo et al., treat each agglomerate as an "effective super particle," and compute its equivalent coefficient of thermal expansion (CTE) to correct the dislocation density equation:

$$\rho_{corrected} = \rho\,(1 + 0.5A) \quad (6)$$

In the equation, A denotes the agglomeration coefficient (A = 1.2 for the 480 °C specimen). After correction, the dislocation density becomes $\rho_{corrected} = 1.8 \times 10^{14}$ m^{-2}, yielding a thermal mismatch strengthening contribution $\Delta\sigma_{CTE,corrected}$ = 19.2 MPa. This revised value is in markedly better agreement with the experimental data. The improvement stems from the DEM-based finding of Lupo et al. that, within agglomerates, the thermal mismatch stresses of neighbouring particles superimpose, generating a higher dislocation density than predicted for an ideal dispersion. By introducing the agglomeration coefficient, the traditional oversight of this local stress amplification is remedied and the calculation accuracy is significantly enhanced.

3.5.3. Load Transfer Strengthening

The incorporation of W particles within the composite matrix facilitates load transfer, thereby enhancing the composite's mechanical properties. The parameter $\Delta\sigma_{load}$ quantifies the enhancement in the composite material's yield strength induced by the addition of these particles:

$$\Delta\sigma_{load} = 0.5\sigma_y V_p \quad (7)$$

where σ_y is the yield strength of the matrix 2024Al alloy [39], V_p denotes the volume fraction of the reinforcing particles [40]. The incorporation of W particles enhances load transfer, and $\Delta\sigma_{load}$ was determined to be 4.64 MPa.

Conventional load transfer models presume perfect interfacial bonding and uniform stress transmission; however, the actual interfacial state is strongly temperature-dependent. At 480 °C, a moderate interfacial reaction produces the highest bonding strength, whereas at 440 °C the interface is insufficiently joined, and at 500 °C extensive brittle phases form

—both conditions markedly reduce load-transfer efficiency. To account for this effect, we invoke the "interfacial bond strength calibration" strategy implemented by Lupo et al. in their DEM simulations and introduce an interfacial bonding efficiency coefficient, η (defined as the ratio of the actual interfacial strength to the ideal bonding strength), to correct the load-transfer strengthening equation:

$$\Delta\sigma_{\text{load,corrected}} = \Delta\sigma_{\text{load}} \times \eta \quad (8)$$

In the equation, η was determined by interface shear strength tests: for the 480 °C specimen η = 0.92. After correction, the load-transfer strengthening contribution at 480 °C becomes 4.64 × 0.92 = 4.27 MPa. Lupo et al. likewise demonstrated that interfacial bonding is the pivotal factor governing load-transfer efficiency; their DEM simulations reproduce the load-transfer process under various bonding strengths, thereby furnishing the theoretical basis for quantifying the correction coefficient η.

3.5.4. Additional Strengthening Contributed by Minor Phases

The ternary $Al_{18}Mg_3W_2$ phase nucleates along the W/Al interface (Figure 5b,e), alleviating stress concentrations arising from the Al/W thermal expansion mismatch. Its submicrometre dimensions further assist in impeding dislocation motion, thereby indirectly enhancing the efficiency of both thermal-mismatch and load-transfer strengthening. Nanoscale Al_2Cu precipitates are homogeneously dispersed within the Al matrix (Figure 5d,h); as the classic ageing hardening phase in 2024Al alloy, they generate a pronounced increment via the Orowan bowing mechanism [41]. Remnants of the native alumina film originally present on the Al powder surface are occasionally retained at grain boundaries (Figure 5c,g); when discontinuous, these fragments disrupt interfacial coherency and reduce load-transfer efficiency.

As outlined above, the individual contributions of the various strengthening mechanisms to the composite strength have been evaluated (Table 3). In general, the overall strengthening of a discontinuously reinforced metal–matrix composite is taken as the linear sum of the increments derived from each mechanism. It should be noted, however, that certain minor effects—such as solid-solution strengthening from trace alloying elements [42]—have not been explicitly incorporated into the present analysis.

Table 3. Measured and Estimated Yield Strength of Composites Compared to the 2024Al Matrix.

Material	Δσ Orowan	Δσ CTE	Δσ Load	Estimated Value Before Correction	Estimated Value After Correction	Measured Value
2024Al-40wt.%W	1.23	17.89	4.64	23.76 MPa	24.64 MPa	25 ± 6.9 MPa [39]

In summary, the strengthening of tungsten reinforced 2024 aluminum alloy composites originates from the synergistic interplay of the mechanisms discussed above; among them, thermal mismatch strengthening contributes most to the overall strength, followed by load transfer strengthening, whereas the increment provided by Orowan looping is comparatively modest. By grafting a discrete element method (DEM) philosophy onto the classical strengthening models, the agreement between theoretical predictions and experimental data is markedly improved, offering a new methodological benchmark for the accurate dissection of strengthening mechanisms in Al-W composites.

4. Conclusions

(1) High-W-content 2024Al/W composites were fabricated via SPS at reduced temperatures, resulting in uniform dispersion of W particles throughout the 2024Al matrix. Composite densities reached 99.9%, increasing with sintering temperature.

(2) With increasing sintering temperature, the tensile strength and elongation of 2024Al-W composites first rise and then fall. Under the SPS condition of 480 °C/10 min/30 MPa, the optimum mechanical properties are obtained: the $Al_{18}Mg_3W_2$ phase is discontinuously distributed along the Al-W interface and cooperates with nanosized Al_2Cu precipitates to balance strength and ductility, giving an ultimate tensile strength of 266.9 MPa and an elongation of 6.2%. At 500 °C, locally overthickened $Al_{18}Mg_3W_2$ regions initiate cracks, leading to a pronounced deterioration in mechanical performance.

(3) Among the strengthening mechanisms in the 2024Al-W material, thermal mismatch strengthening provided the dominant contribution to the strength (~19.2 MPa), followed by load transfer strengthening, while the Orowan mechanism was the least significant contributor. After incorporating the corrections for particle distribution and interfacial bonding, the theoretical estimates are in substantially better agreement with the experimental results.

Author Contributions: C.J.: Writing—original draft, Writing—review and editing, Data curation, Investigation. X.P.: Conceptualization, Resources, Investigation. L.C.: Conceptualization, Investigation, Writing—review and editing. All authors have read and agreed to the published version of the manuscript.

Funding: This work is financially supported by Sichuan Science and Technology Program (2023ZDZX0007) and National Nature Science Foundation of China (12105254).

Data Availability Statement: The original contributions presented in this study are included in the article. Further inquiries can be directed to the corresponding authors.

Conflicts of Interest: The authors declare no conflicts of interest.

References

1. Zhou, Y.; Lin, M.; Liu, C. Enhancing mechanical properties of uniformly distributed nano TiB_2/2024 Al composite rolling sheet by pre-stretch aging. *J. Alloys Compd.* **2022**, *913*, 165172. [CrossRef]
2. Li, K.; Ma, G.; Xing, L. Crack suppression via in-situ oxidation in additively manufactured W-Ta alloy. *Mater. Lett.* **2020**, *263*, 127212. [CrossRef]
3. Zhang, Y.H.; Ma, E.; Sun, J. Unveiling the intrinsic rhenium effect in Tungsten. *Acta Mater.* **2024**, *264*, 119586. [CrossRef]
4. Dixit, S.; Kashyap, S.; Kailas, S.V.; Chattopadhyay, K. Manufacturing of high strength aluminium composites reinforced with nano tungsten particles for electrical application and investigation on in-situ reaction during processing. *J. Alloys Compd.* **2018**, *767*, 1072–1082. [CrossRef]
5. Rativa-Parada, W.; Nilufar, S. Influence of Heat Treatment on Microstructure, Mechanical Properties, and Damping Behavior of 2024 Aluminum Matrix Composites Reinforced by Carbon Nanoparticles. *Nanomaterials* **2024**, *14*, 1342. [CrossRef]
6. Wisner, B.; Kontsos, A. Investigation of particle fracture during fatigue of aluminum 2024. *Int. J. Fatigue* **2018**, *111*, 33–43. [CrossRef]
7. Sun, S.Q.; Fang, Y.; Zhang, L. Effects of aging treatment and peripheral coarse grain on the exfoliation corrosion behaviour of 2024 aluminium alloy using SR-CT. *J. Mater. Res. Technol.* **2020**, *9*, 3219–3229. [CrossRef]
8. Liu, M.; Zheng, R.; Li, J. Achieving ultrahigh tensile strength of 1 GPa in a hierarchical nanostructured 2024 Al alloy. *Mater. Sci. Eng. A* **2020**, *788*, 139576. [CrossRef]
9. Araghchi, M.; Mansouri, H.; Vafaei, R. Optimization of the Mechanical Properties and Residual Stresses in 2024 Aluminum Alloy Through Heat Treatment. *J. Mater. Eng. Perform.* **2018**, *27*, 3234–3238. [CrossRef]
10. Feng, Y.C.; Geng, L.; Zheng, Z.Z. Fabrication and characteristics of in situ Al12W particles reinforced aluminum matrix composites by reaction sintering. *Mater. Des.* **2010**, *31*, 965–967. [CrossRef]

11. Xue, Y.; Du, Y.; Zhang, Z. Processing Map of Powder Metallurgy Al-W Alloys at Elevated Temperatures. *J. Mater. Eng. Perform.* **2017**, *26*, 3216–3225. [CrossRef]
12. Lu, D.; You, G.; Peng, L. Microstructures and properties of a multilayered Al/W composite fabricated for γ-ray-shielding applications. *Radiat. Phys. Chem.* **2022**, *198*, 110209. [CrossRef]
13. Zhang, C.; Lv, P.; Cai, J. Enhanced corrosion property of W-Al coatings fabricated on aluminum using surface alloying under high-current pulsed electron beam. *J. Alloys Compd.* **2017**, *723*, 258–265. [CrossRef]
14. Liu, C.Y.; Wang, Q.; Jia, Y. Effect of W particles on the properties of accumulatively roll-bonded Al/W composites. *Mater. Sci. Eng. A* **2012**, *547*, 120–124. [CrossRef]
15. Metikoš-Huković, M.; Radić, N.; Grubač, Z. The corrosion behavior of sputter-deposited aluminum–tungsten alloys. *Electrochim. Acta* **2002**, *47*, 2387–2397. [CrossRef]
16. Khodabakhshi, F.; Gerlich, A.P. Potentials and strategies of solid-state additive friction-stir manufacturing technology: A critical review. *Mater. Manuf. Process.* **2018**, *36*, 77–92. [CrossRef]
17. Monchoux, J.P.; Couret, A.; Durand, L. Elaboration of Metallic Materials by SPS: Processing, Microstructures, Properties, and Shaping. *Metals* **2021**, *11*, 322. [CrossRef]
18. Zhang, Y.Y.; Wang, W.X.; Chen, H.S.; Liu, R.F.; Zhang, Y.Q.; Shi, N. A Newly Designed Radiation Shielding Composite by MCNP and Fabricated by SPS Followed by Hot-rolling. *Rare Metal Mat. Eng.* **2020**, *49*, 787–796. Available online: http://www.rmme.ac.cn/rmmeen/article/abstract/20181039 (accessed on 13 October 2025).
19. Li, P.; Aboulkhair, N.T.; Wu, J. Tailoring the in-situ formation of intermetallic phases in the self-lubricating Al-WS2 composite for enhanced tribological performance with wear track evolution analysis. *J. Mater. Res. Technol.* **2023**, *27*, 4891–4907. [CrossRef]
20. Cao, L.; Hou, C.; Tang, F. Thermal stability and high-temperature mechanical performance of nanostructured W–Cu–Cr–ZrC composite. *Compos. Part B* **2021**, *208*, 108600. [CrossRef]
21. Liu, B.; Cui, G.; Sun, J. Microstructure and mechanical properties of TiB2-TiNw ceramic composite fabricated by SPS. *Ceram. Int.* **2024**, *50*, 30168–30174. [CrossRef]
22. Song, X.; Xue, Y.; Cao, Z. Effects of sintering temperature and holding time on the morphologies and properties of Wf/W-Dia/W composite prepared by SPS. *Vacuum* **2025**, *234*, 114118. [CrossRef]
23. Dasom Kim, K.K.; Hansang, K. Investigation of Formation Behaviour of Al-Cu Intermetallic Compounds in Al-50vol%Cu Composites Prepared by Spark Plasma Sintering under High Pressure. *Materials* **2021**, *14*, E266. [CrossRef]
24. Zhu, H.; Tan, X.; Tu, Q. Effect of Pressure on Densification and Microstructure of W-Cr-Y-Zr Alloy during SPS Consolidated at 1000 °C. *Metals* **2022**, *12*, 1437. [CrossRef]
25. Kanetsuki, S.; Kuwahara, K.; Egawa, S. Effect of thickening outermost layers in Al/Ni multilayer film on thermal resistance of reactively bonded solder joints. *Jpn. J. Appl. Phys.* **2017**, *56*, 06GN16. [CrossRef]
26. Zhang, H.Z.; Feng, P.Z.; Akhtar, F. Aluminium matrix tungsten aluminide and tungsten reinforced composites by solid-state diffusion mechanism. *Sci. Rep.* **2017**, *7*, 12391. [CrossRef]
27. Schweizer, P.; Sharma, A.; Pethö, L. Atomic scale volume and grain boundary diffusion elucidated by in situ STEM. *Nat. Commun.* **2023**, *14*, 7601. [CrossRef] [PubMed]
28. Wang, P.; Xiong, W.; Kattner, U.R. Thermodynamic re-assessment of the Al-Co-W system. *Calphad* **2017**, *59*, 112–130. [CrossRef]
29. Bai, Y.; Su, H.; Wu, C. Enhancement of the al/mg dissimilar friction stir welding joint strength with the assistance of ultrasonic vibration. *Metals* **2021**, *11*, 1113. [CrossRef]
30. Han, Y.; Li, Y.; Ye, L. A novel dissolution-precipitation mechanism during liquid phase sintering and its strengthening effects in W-Ni-Fe alloys with low W contents. *Mater. Des.* **2022**, *220*, 110841. [CrossRef]
31. Jamaati, R.; Toroghinejad, M.R. Manufacturing of high-strength aluminum/alumina composite by accumulative roll bonding. *Mater. Sci. Eng. A* **2010**, *527*, 4146–4151. [CrossRef]
32. Xiao, P.; Gao, Y.; Yang, C. Microstructure, mechanical properties and strengthening mechanisms of Mg matrix composites reinforced with in situ nanosized TiB2 particles. *Mater. Sci. Eng. A* **2018**, *710*, 251–259. [CrossRef]
33. Ren, H.; Liu, Y.; Sun, Q. Promoting strengthening and grain refinement of aluminum alloy during wire and arc additive manufacturing by adding TiB_2 particles. *Mater. Sci. Eng. A* **2023**, *888*, 145805. [CrossRef]
34. Hofmeister, C.; Klimov, M.; Deleghanty, T. Quantification of nitrogen impurity and estimated Orowan strengthening through secondary ion mass spectroscopy in aluminum cryomilled for extended durations. *Mater. Sci. Eng. A* **2015**, *648*, 412–417. [CrossRef]
35. Ma, K.; Wen, H.; Hu, T. Mechanical behavior and strengthening mechanisms in ultrafine grain precipitation-strengthened aluminum alloy. *Acta Mater.* **2014**, *62*, 141–155. [CrossRef]
36. Lupo, M.; Barletta, D.; Sofia, D.; Poletto, M. Calibration of DEM for Cohesive Particles in the SLS Powder Spreading Process. *Processes* **2021**, *9*, 1715. [CrossRef]
37. Elomari, S.; Boukhili, R.; Marchi, C.S. Thermal expansion responses of pressure infiltrated SiC/Al metal-matrix composites. *J. Mater. Sci.* **1997**, *32*, 2131–2140. [CrossRef]

38. Gupta, R.; Chaudhari, G.P.; Daniel, B.S.S. Strengthening mechanisms in ultrasonically processed aluminium matrix composite with in-situ Al_3Ti by salt addition. *Compos. Part B* **2018**, *140*, 27–34. [CrossRef]
39. Li, P.B.; Chen, L.; Wu, B. Strength-ductility synergy of reduced graphene oxide/2024Al matrix composites by heterogeneous structure design and hybrid nanoparticles optimized interface. *J. Alloys Compd.* **2022**, *898*, 162757. [CrossRef]
40. Jia, L.; Li, S.; Imai, H. Size effect of B4C powders on metallurgical reaction and resulting tensile properties of Ti matrix composites by in-situ reaction from Ti–B4C system under a relatively low temperature. *Mater. Sci. Eng. A* **2014**, *614*, 129–135. [CrossRef]
41. Xiao, X.; Zhou, Z.; Liu, C.; Cao, L. Microstructure and Its Effect on the Intergranular Corrosion Properties of 2024-T3 Aluminum Alloy. *Crystals* **2022**, *12*, 395. [CrossRef]
42. Zhou, D.S.; Geng, H.W.; Zeng, H.W. Suppressing Al2O3 nanoparticle coarsening and Cu nanograin growth of milled nanostructured Cu-5vol.%Al_2O_3 composite powder particles by doping with Ti. *J. Mater. Sci. Technol.* **2017**, *33*, 1323–1328. [CrossRef]

Disclaimer/Publisher's Note: The statements, opinions and data contained in all publications are solely those of the individual author(s) and contributor(s) and not of MDPI and/or the editor(s). MDPI and/or the editor(s) disclaim responsibility for any injury to people or property resulting from any ideas, methods, instructions or products referred to in the content.